Mechanical Property Characterization of Single Scan Laser Tracks of Nickel Superalloy 625 by Nanoindentation

Jordan S. Weaver, Meir Kreitman, Jarred C. Heigel and M. Alkan Donmez

Abstract Laser-based additive manufacturing of metals relies on many micro-sized welds to build a part. A simplified, well-studied case of this process is a single scan of the laser across a single layer of powder. However, there is a lack of mechanical property measurements of the tracks produced in such experiments. Nanoindentation measurements on laser track cross sections of nickel superalloy 625 reveal hardness differences between the track melt pool and base material as well as variations with laser scan speed. There is a change from ≈5.5 GPa in the track melt pool to ≈4.8 GPa in the base material for laser settings of 195 W and 800 mm s^{-1}. In comparison, the increase in hardness in the melt pool is not observed for settings of 195 W and 200 mm s^{-1}. It is believed that the difference in thermal histories supported by thermographic measurements causes a difference in the dislocation density in the melt pool. This results in a difference in hardness between the two tracks. The effects of the local crystal orientation, dendritic spacing, and residual stress are considered in the interpretation of results.

Keywords Additive manufacturing · Hardness · Residual stress · Microstructure · Electron backscatter diffraction

Introduction

Laser-based additive manufacturing of metals relies on the process of a laser to melt feedstock material to build a component layer by layer. This process can be broken down to the fundamental step of a single scan of the laser across a bare plate or a single layer of powder. These rather simple experiments have proven highly useful for developing models that can predict temperature, residual stress, melt pool geometry, and microstructure (e.g., [1–8]). Less emphasis has been placed on predicting mechanical properties (e.g., hardness) of single scan laser tracks. This may be in part due to the difficulties associated with testing and interpreting mechanical performance over

J. S. Weaver (✉) · M. Kreitman · J. C. Heigel · M. A. Donmez
Engineering Laboratory, National Institute of Standards and Technology, 100 Bureau Dr, Gaithersburg, MD 20878, USA
e-mail: jordan.weaver@nist.gov

The Minerals, Metals & Materials Society (ed.), *TMS 2019 148th Annual Meeting & Exhibition Supplemental Proceedings*, The Minerals, Metals & Materials Series, https://doi.org/10.1007/978-3-030-05861-6_24

micrometer length scales. While understanding the mechanical performance of built components is the goal, there is still a lot to gain from understanding the mechanical properties inside single scan laser tracks. In such experiments, it is possible to clearly link the mechanical response to the laser power and scan speed without the complications of the compound thermal history that exists in a component.

Materials and Methods

Nickel superalloy 625 (IN625) was chosen because it is widely used in additive manufacturing and industrial applications. IN625 plate of approximately 3.2 mm thick was polished to 400 grit and annealed at 870 °C for 1 h in vacuum. A single layer of EOS[1] IN625 powder was hand spread with an approximate layer thickness of 36 μm prior to exposing to the laser. Single scans on the single layer of powder were made following procedures given in Ref. [8] using a commercial EOS M270D[1] laser bed powder fusion machine. Each single scan was sufficiently spaced to reduce the influence on neighboring scans and sufficiently long to reach a steady state. Two different combinations of laser power and scan speed were investigated: 195 W at 200 mm s^{-1} and 195 W at 800 mm s^{-1}. The estimated laser spot size for these experiments and the single scan laser tracks in Ref. [8] is 100 μm. This is different than the estimated spot size of 188 μm for experiments in Ref. [3]. The difference in spot size and the addition of a layer of powder should be kept in mind when comparing the melt pool geometries from this study to Ref. [3].

Single scan laser tracks were cross sectioned as shown in Fig. 1a, b. The cross sections were mounted and metallographically prepared using a final vibratory polish with 0.02 μm colloidal silica. Nanoindentation was performed using an MTS (Keysight) Nanoindenter XP[1] on cross sections in the melt pool regions and far from the melt pools as shown in Fig. 1b. Here, we use the term melt pool to describe the material that was melted by the laser and resolidified. A final indentation depth of 300 nm was chosen to reduce the spacing between indents to 10 μm allowing for at least several indents inside the melt pool. This produces residual indents on the order of a micrometer (see Fig. 1c, d) which are influenced by the local crystal structure. The local crystal structure at each indentation site was determined from electron backscatter diffraction (EBSD) using a JOEL JSM7100[1] field-emission scanning electron microscope (SEM) and Oxford[1] EBSD detector (Fig. 1c, d). The positions of indents with respect to the surface and melt pool geometry were determined from optical micrographs before and after etching using a Zeiss LSM 800[1] optical microscope. Etching with aqua regia was necessary to reveal the melt pool boundary to identify indents as either inside or outside the melt pool.

[1]Certain commercial equipment, instruments, or materials are identified in this paper in order to specify the experimental procedure adequately. Such identification is not intended to imply recommendation or endorsement by the National Institute of Standards and Technology, nor is it intended to imply that the materials or equipment identified are necessarily the best available for the purpose.

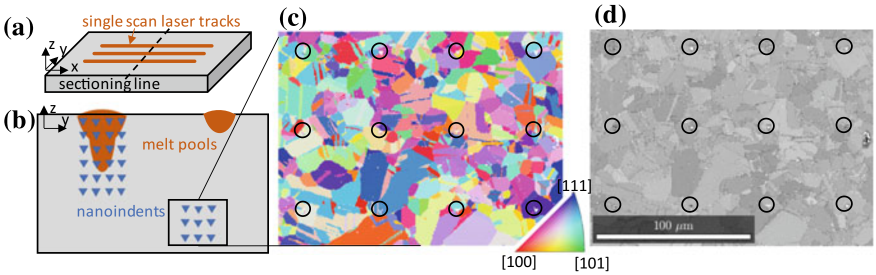

Fig. 1 **a** Schematic of single scan laser tracks on a single layer of powder, **b** schematic of single track laser scan cross sections with nanoindents. The melt pool size/shape varies depending on the laser power and scan speed. Indent size is exaggerated. **c** EBSD inverse pole figure map of the base material far from the laser tracks containing circled indents to 300 nm displacement, **d** corresponding band contrast image. The scale bar is the same for (**c**) and (**d**)

Nanoindentation was performed with a diamond Berkovich tip to a final displacement of 300 nm. The strain rate, which is the loading rate divided by the load, was held constant at 0.05 s^{-1}. The continuous stiffness method (CSM), which superimposes a small oscillatory loading signal on the monotonic loading signal, was employed with a displacement amplitude of 2 nm and frequency of 45 Hz. The CSM allows for the determination of the unloading stiffness, S, throughout the test from many small unloads [9]. Unloading is necessary to determine the contact area, A, effective modulus, E_{eff}, and hardness, H, in accordance with the Oliver–Pharr analysis [10]. The hardness in Eq. (1) is simply the load divided by the cross-sectional area. The area function is determined from tests of fused quartz [10]. All eight area function coefficients were used with an emphasis on data at shallower depths <1000 nm. The effective modulus, Eq. (2), depends on the stiffness, contact area, and a correction factor β. A value of 1.034 was used in the area function calibration and analysis [10]. The effective modulus, Eq. (3), is the elastic response of the indenter tip and sample designated with subscripts i and s, respectively, which is dependent on the moduli, E, and Poisson ratios, v. A modulus and Poisson's ratio of 1140 GPa and 0.07, respectively, were used for the diamond tip. A sample Poisson's ratio of 0.31 was used to determine the sample modulus. This value is the Voigt–Reuss–Hill Poisson's ratio [11] based on available elastic constants of nickel superalloy 625 [12]. Note that the sample modulus, E_s, is not the single crystal Young's modulus. A more rigorous account of elastic anisotropy of cubic crystals during indentation should be followed if this is desired (see Refs. [13, 14]).

$$H = \frac{P}{A} \tag{1}$$

$$E_{eff} = \frac{\sqrt{\pi} S}{2\beta\sqrt{A}} \tag{2}$$

$$\frac{1}{E_{eff}} = \frac{1 - v_s^2}{E_s} + \frac{1 - v_i^2}{E_i} \tag{3}$$

Indentation size effects, where the hardness is higher at shallower depths is commonly reported in metals and alloys [15]. A model that can be used to estimate the intrinsic hardness or hardness at infinite depth is the Nix–Gao model using Eq. (4) [15]. The intrinsic hardness, H_0, and length scale parameter, h^*, are determined from a regression of the hardness, H, and displacement, h, data.

$$\frac{H}{H_0} = \sqrt{1 - \frac{h^*}{h}} \tag{4}$$

The apparent indentation size effect at very shallow depths <200 nm is sensitive to the sharpness of the tip, sample preparation, etc. [16]. The tests on the laser track cross sections were limited to 300 nm to reduce the spacing between indents and to fit many into the melt pool. This leaves only a small portion of data (200–300 nm displacement) to determine the intrinsic hardness and length scale parameter. Tests on the annealed plate up to 1000 nm displacement were also analyzed. The mean values using data from 200 to 300 nm and 200 to 1000 nm were similar while the variance was significantly higher for 200–300 nm. This should be kept in mind when interpreting the Nix–Gao parameters from a limited range of indentation depth.

Results and Discussion

Figure 2 shows the shape and grain structure of the laser track cross sections from EBSD and optical micrographs. The most obvious difference between the two tracks is in the size of the melt pool with clear keyholing occurring for slower scan speed. The melt pool boundaries on the EBSD maps are approximations based on the formation of the elongated grain structure in the melt pool. The actual melt pool boundary is determined from the optical images of etched samples. Nanoindents can be seen on the band contrast maps (Fig. 2b, e) as a uniform grid of black spots with 10 μm spacing. They are also faintly present in the optical images which allowed for categorizing indents as either inside the melt, outside the melt, or on the border of the two regions.

Figure 3 shows the nanoindentation trends for one laser track, 195 W at 800 mm s^{-1}. The average hardness, Fig. 3a, and sample modulus, Fig. 3b, for each test were determined using data between 275 nm and 300 nm displacement. The Nix–Gao model values, Fig. 3c, d, were determined by a regression to data between 200 and 300 nm displacement. The x-axis in these plots is the perpendicular distance each indent is from the original surface of the plate. Some indents can have a negative position if they landed in the solidified powder layer above the plate's original surface. In addition, each data point or indent is categorized as either inside the melt pool, outside the melt pool, or on the border. Indents were considered on the border if they fell directly on the melt pool boundary or fell relatively close to the boundary (≈3 μm). There is a clear increase in hardness and slightly lower modulus in the melt pool (Fig. 3a) compared to outside the melt pool. This is likely due to a combination

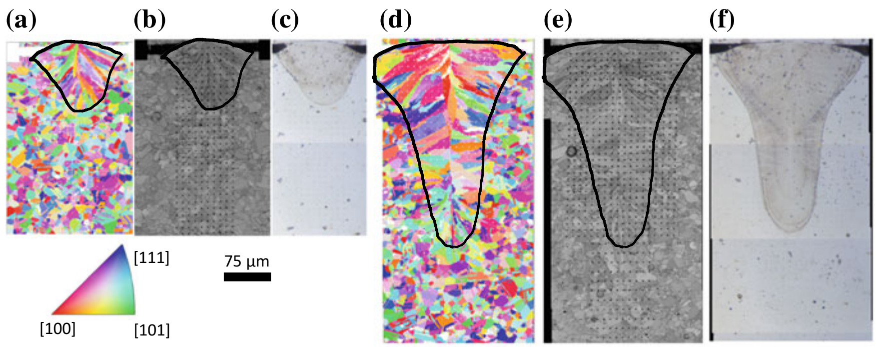

Fig. 2 **a** EBSD inverse pole figure, **b** EBSD band contrast, and **c** the corresponding optical micrograph of laser track cross sections after nanoindentation for 195 W at 800 mm s^{-1}. **d** EBSD inverse pole figure, **e** EBSD band contrast, and **f** the corresponding optical micrograph of laser track cross sections after nanoindentation for 195 W at 200 mm s^{-1}

of increased dislocation density, the dendritic microstructure, and residual stresses compared to the annealed plate where these do not exist (dendrites, residual stress) or are minimized (dislocation density). The temperature gradient that occurs in the melt pool during the rapid solidification produces internal stresses. These stresses during the solidification process are likely high enough to generate dislocations through local plastic deformation and/or crystal orientation gradients. An increase in dislocation density will increase the measured hardness (i.e., Taylor hardening law). The intrinsic hardness, Fig. 3c is also higher in the melt pool for the same reasons and the length scale parameter is reduced (i.e., the indentation size effect is reduced). Other scenarios where the intrinsic hardness increases and the length scale parameter reduces are in cold-worked [15] and radiation-damaged materials [17]. In both these scenarios, there is an increase in the dislocation density in the material.

The residual internal stresses in the material after the material solidifies and cools can also affect the hardness as well as the measured modulus [18]. Generally, a compressive residual stress in the indentation plane will increase the measured hardness and a tensile stress will reduce the hardness [18]. Changes in the measured sample modulus are a good indicator of this type of residual stress and severity, with compressive residual stresses increasing the effective modulus and tensile residual stress decreasing the effective modulus [18]. However, Ref. [18] found that the measured changes in modulus and hardness with residual stress went away when the contact area was determined from images of residual indents rather than the unloading stiffness. The conclusions are likely dependent on the tip geometry, indentation depth, and material making it difficult to directly apply them to this study. Another solution to this issue that does not require measuring the residual indent area is to use the known modulus to correct the data [19]. Here, we leave the measurements as is and caution that whenever the modulus values deviate from the base material without a physical reason such as the case of residual stresses, there may be errors in the hardness associated with errors in the contact area. This issue requires further investigation.

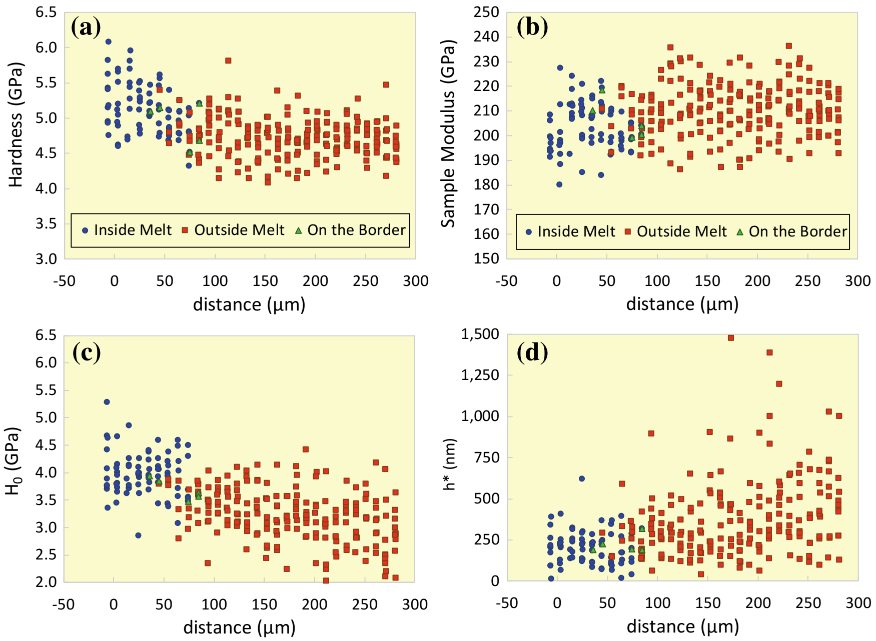

Fig. 3 Indentation property versus the distance of each indent from the laser track surface for 195 W at 800 mm s^{-1}: **a** hardness at 275–300 nm displacement, **b** modulus at 275–300 nm displacement, **c** intrinsic hardness, H_0, determined from 200 to 300 nm displacement and **d** length scale parameter, h^*, determined from 200 to 300 nm displacement. The blue circles are indents that fell inside the melt pool, green triangles were on the border, and the red squares fell outside the melt pool

Figure 4 shows the indentation trends for laser track 195 W at 800 mm s^{-1} reduced to tests inside similar grain orientations. Grains were defined from EBSD data based on a misorientation angle <5°. Grains with a crystal normal within 10° of the (2 2 11) direction were isolated. This crystal plane was chosen so that several grains inside and outside the melt pool could be compared. Some of the indents considered are very close to grain boundaries. A stricter criterion would be to only consider indents that are approximately three times the residual indent diameter away from any grain boundaries; however, this would eliminate most of the tests. Rather we consider tests if they did not fall directly on any grain boundaries and meet the orientation requirement. The reduced data based on similar grain orientations shows the same trends as the grid of indents which does not consider grain orientation. This means the grain orientation does not have a significant effect on the nanohardness trends. We also note that even inside the same grain in the melt pool (e.g., indent numbers 4, 18, and 21), the hardness and modulus measurements vary. For these reasons, the arrays of indents are sufficient for comparison of different laser tracks. This may not be the case for crystals with greater plastic anisotropy (e.g., hexagonal crystals) or indentation with tip geometries that produce less plastic deformation (e.g., spherical tips).

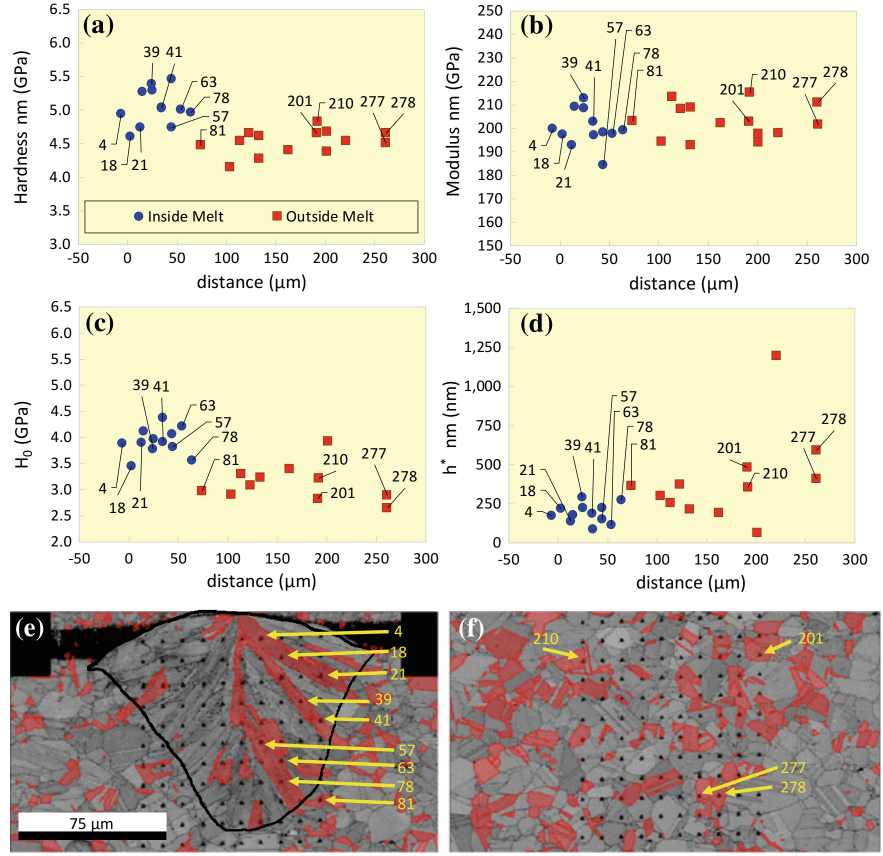

Fig. 4 Indentation property versus the distance of indents inside grains with a crystal plane <10° from (2 2 11) for the laser track 195 W at 800 mm s^{-1}: **a** hardness, **b** modulus, **c** intrinsic hardness, H_0, and **d** length scale parameter, h^*. The blue circles are indents that fall inside the melt pool, and the red squares fall outside the melt pool. (**e**, **f**) EBSD band contrast images with grains shaded red that meet orientation criterion. A selection of indents is labeled with their respective number. Indents 4, 18, and 21 are inside one grain. Indents 39 and 41 are inside one grain. Indents 57, 63, 78, and 81 are also inside one grain

Figure 5 shows a direct comparison of the hardness and modulus for the two laser tracks at a power of 195 W and scan speeds of 800 and 200 mm s^{-1}. The dashed lines in the plots are based on one standard deviation above and below the mean of 95 indents on the annealed plate far from the tracks. The increase in hardness on the track with scan speed of 800 mm s^{-1} is not seen in the track with scan speed of 200 mm s^{-1}. To understand this, we consider the difference in the thermal history between the two tracks. Radiant temperature measurements along tracks and estimated cooling rates were made using the procedures in Ref. [8] which show that the temperature gradients, change in temperature over distance, trailing the melt pool are similar between the two tracks. The cooling rate, change in temperature

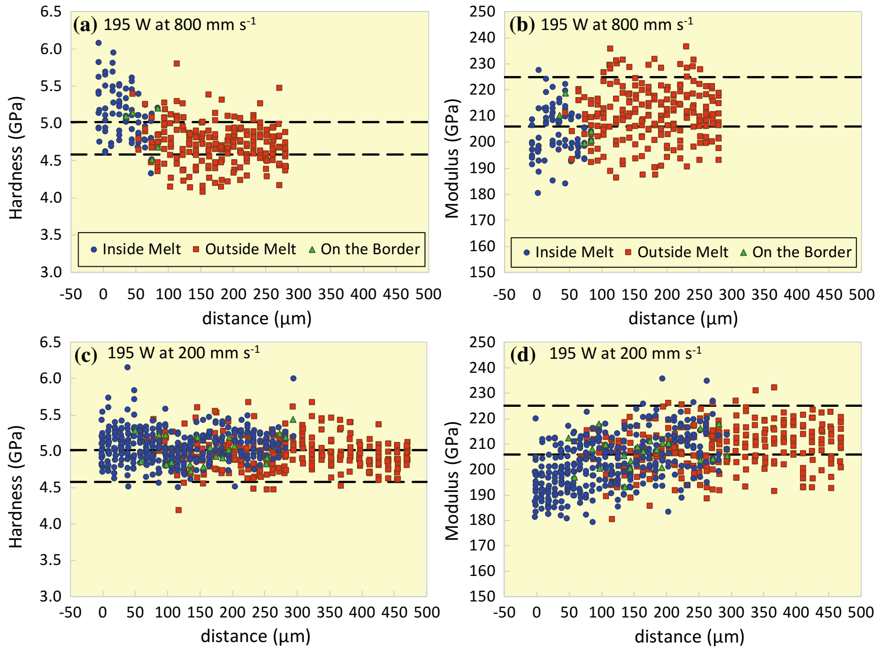

Fig. 5 Comparison of indentation hardness (**a**, **c**) and sample modulus (**b**, **d**) for laser tracks 195 W. **a**, **b** 800 mm s^{-1}, **c**, **d** 200 mm s^{-1}. The dotted lines are ± one standard deviation of the mean for 95 indents on the annealed plate far from the tracks. **a**, **b** contain 295 indents and **c**, **d** contain 690 indents

over time, is roughly the temperature gradient multiplied by the laser scan speed. This means that the estimated cooling rate scales with the laser scan speed; the cooling rate is approximately four times greater for the 800 mm s^{-1} track compared to the 200 mm s^{-1} track. A difference in cooling rate will produce a difference in the dendritic spacing in the melt pool which can be estimated from phase field simulations as 0.2 μm and 0.43 μm for the 800 mm s^{-1} and 200 mm s^{-1} scan speeds, respectively [3]. The indents are on the order of 1 micrometer such that in both cases it is likely probing multiple dendrites. We reason that the difference in dendritic spacing is not a significant factor in the comparison of hardness between the two tracks. It should be noted that the radiant temperature measurements are surface measurements and do not measure the temperature gradient or cooling rate along the depth of the melt pool. Based on the radiant temperature measurements and the size of the melt pool cross sections, we reason that the thermal histories are sufficiently different to cause differences in the dislocation density. A greater cooling rate, possibly steeper temperature gradient along the depth of the melt pool, and subsequent greater dislocation density inside the 800 mm s^{-1} track would explain why the hardness is higher in the 800 mm s^{-1} track compared to the 200 mm s^{-1} track.

The modulus is reduced for both tracks in the melt pool to a similar level. Any error in hardness due to this effect, as discussed earlier, likely does not have a significant effect in the comparison between tracks. The uncertainty in the modulus and hardness values is estimated based on Ref. [20] which found an average uncertainty (one standard deviation) among individual participants in a round robin study to be 4% of the average hardness and 5% of the average modulus. For comparison, one standard deviation of 95 measurements on annealed plate material far from the laser tracks was 0.22 GPa or 4.7% of the average hardness and 10 GPa or 4.4% of the average modulus.

Summary

Two different single scan laser tracks on a single layer of nickel superalloy 625 powder were cross sectioned and characterized with Berkovich nanoindentation. EBSD was used to isolate grain orientation effects and optical microscopy was used to determine position of indents relative to the surface and melt pool boundary. There are several findings from these experiments which are as follows:

1. The hardness inside the melt pool for 195 W, 800 mm s^{-1} is higher than the annealed plate likely due to an increase in dislocation density in the melt pool because of the rapid cooling and temperature gradients during the solidification process.
2. Isolating indents based on similar grain orientations show the same trend across the melt pool as large arrays of indents. Crystal orientation effects on the indentation response are not a significant factor in interpreting this set of experiments.
3. The comparison of the hardness and modulus for laser tracks of 195 W at 800 and 200 mm s^{-1} reveals that the hardness is higher inside the melt pool for a scan speed of 800 mm s^{-1}. The increased cooling rate and possibly steeper temperature gradient along the melt pool depth in the 800 mm s^{-1} track increase the dislocation density and subsequent hardness.
4. The measured modulus is reduced in the laser tracks likely due to residual stresses. This might cause the hardness to be underestimated due to an error in the determination of the contact area. The reduction in modulus is similar for both tracks and does not affect the comparison between the two different tracks.

Acknowledgements We wish to thank Will Osborn and Maureen Williams of the Materials Measurement Laboratory at NIST for their help with EBSD. We are very appreciative of Mark Stoudt of the Materials Measurement Laboratory at NIST for etching samples and discussing the many aspects of additive nickel superalloy 625. We are also grateful of Lyle Levine and Will Osborn of the Materials Measurement Laboratory at NIST for bringing to our attention the need to do these experiments. Meir Kreitman wishes to acknowledge support from the University of Maryland and the NIST Summer Undergraduate Research Fellowship (SURF) program.

References

1. Hussein A, Hao L, Yan C, Everson R (2013) Finite element simulation of the temperature and stress fields in single layers built without-support in selective laser melting. Mater Des (1980–2015) 52:638–647
2. Keller T, Lindwall G, Ghosh S, Ma L, Lane BM, Zhang F, Kattner UR, Lass EA, Heigel JC, Idell Y, Williams ME, Allen AJ, Guyer JE, Levine LE (2017) Application of finite element, phase-field, and CALPHAD-based methods to additive manufacturing of Ni-based superalloys. Acta Mater 139:244–253
3. Ghosh S, Ma L, Levine LE, Ricker RE, Stoudt MR, Heigel JC, Guyer JE (2018) Single-track melt-pool measurements and microstructures in Inconel 625. JOM 70(6):1011–1016
4. Montgomery C, Beuth J, Sheridan L, Klingbeil N (2015) Process mapping of Inconel 625 in laser powder bed additive manufacturing. In: Solid freeform fabrication symposium, pp 1195–1204
5. Heigel JC, Lane BM (2018) Measurement of the melt pool length during single scan tracks in a commercial laser powder bed fusion process. J Manuf Sci Eng 140(5):051012–051012-7
6. Akram J, Chalavadi P, Pal D, Stucker B (2018) Understanding grain evolution in additive manufacturing through modeling. Addit Manuf 21:255–268
7. Ma L, Fong J, Lane B, Moylan S, Filliben J, Heckert A, Levine L (2015) Using design of experiments in finite element modeling to identify critical variables for laser powder bed fusion. In: International solid freeform fabrication symposium, laboratory for freeform fabrication and the University of Texas Austin, TX, USA, pp 219–228
8. Heigel JC, Lane BM (2017) The effect of powder on cooling rate and melt pool length measurements using in situ thermographic techniques. In: Solid freeform fabrication symposium
9. Hay J, Agee P, Herbert E (2010) Continuous stiffness measurement during instrumented indentation testing. Exp Tech 34(3):86–94
10. Oliver WC, Pharr GM (2004) Measurement of hardness and elastic modulus by instrumented indentation: advances in understanding and refinements to methodology. J Mater Res 19(1):3–20
11. Hill R (1952) The elastic behaviour of a crystalline aggregate. Proc Phys Soc Sect A 65(5):349
12. Wang Z, Stoica AD, Ma D, Beese AM (2016) Diffraction and single-crystal elastic constants of Inconel 625 at room and elevated temperatures determined by neutron diffraction. Mater Sci Eng A 674:406–412
13. Vlassak JJ, Nix WD (1994) Measuring the elastic properties of anisotropic materials by means of indentation experiments. J Mech Phys Solids 42(8):1223–1245
14. Vlassak JJ, Nix WD (1993) Indentation modulus of elastically anisotropic half-spaces. Philos Mag A 67(5):1045–1056
15. Nix WD, Gao HJ (1998) Indentation size effects in crystalline materials: a law for strain gradient plasticity. J Mech Phys Solids 46(3):411–425
16. Pharr GM, Herbert EG, Gao YF (2010) The indentation size effect: a critical examination of experimental observations and mechanistic interpretations. Annu Rev Mater Res 40:271–292
17. Hosemann P, Shin C, Kiener D (2015) Small scale mechanical testing of irradiated materials. J Mater Res 30(9):1231–1245
18. Tsui TY, Oliver WC, Pharr GM (2011) Influences of stress on the measurement of mechanical properties using nanoindentation: Part I. Experimental studies in an aluminum alloy. J Mater Res 11(3):752–759
19. Hou X, Jennett N (2017) A method to separate and quantify the effects of indentation size, residual stress and plastic damage when mapping properties using instrumented indentation. J Phys D Appl Phys 50(45):455304
20. Read DT, Keller RR, Barbosa N, Geiss R (2007) Nanoindentation round robin on thin film copper on silicon. Metall Mat Trans A 38(13):2242–2248